Author Manuscript
Accepted for publication in a peer-reviewed journal

NIST National Institute of Standards and Technology • U.S. Department of Commerce

Published in final edited form as:
Nano Res. 2019 ; 12: . doi:10.1007/s12274-018-2202-x.

Nanoscale Chemical Imaging of Individual, Chemotherapeutic Cytarabine-loaded Liposomal Nanocarriers

Karin Wieland[1], **Georg Ramer**[2,3], **Victor U. Weiss**[4], **Guenter Allmaier**[4], **Bernhard Lendl**[1], and **Andrea Centrone**[2]

[1]Institute of Chemical Technologies and Analytics. Research Division Environmental, Process Analytics and Sensors, TU Wien, Vienna 1060, Austria.

[2]Center for Nanoscale Science and Technology, National Institute of Standards and Technology, Gaithersburg, MD 20899, USA

[3]Institute for Research in Electronics and Applied Physics, University of Maryland, College Park, MD 20742, USA

[4]Institute of Chemical Technologies and Analytics. Research Division Instrumental and Imaging Analytical Chemistry, TU Wien, Vienna 1060, Austria.

Abstract

Dosage of chemotherapeutic drugs is a tradeoff between efficacy and side-effects. Liposomes are nanocarriers that increase therapy efficacy and minimize side-effects by delivering otherwise difficult to administer therapeutics with improved efficiency and selectivity. Still, variabilities in liposome preparation require assessing drug encapsulation efficiency at the single liposome level, an information that, for non-fluorescent therapeutic cargos, is inaccessible due to the minute drug load per liposome. Photothermal induced resonance (PTIR) provides nanoscale compositional specificity, up to now, by leveraging an atomic force microscope (AFM) tip contacting the sample to transduce the sample's photothermal expansion. However, on soft samples (e.g. liposomes) PTIR effectiveness is reduced due to the likelihood of tip-induced sample damage and inefficient AFM transduction. Here, individual liposomes loaded with the chemotherapeutic drug cytarabine are deposited intact from suspension via nES-GEMMA (nano-electrospray gas-phase electrophoretic mobility molecular analysis) collection and characterized at the nanoscale with the chemically-sensitive PTIR method. A new tapping-mode PTIR imaging paradigm based on heterodyne detection is shown to be better adapted to measure soft samples, yielding cytarabine distribution in individual liposomes and enabling classification of empty and drug-loaded liposomes. The measurements highlight PTIR capability to detect ≈ 10^3 cytarabine molecules (≈ 1.7 zmol) label-free and non-destructively.

Address correspondence to A. Centrone, andrea.centrone@nist.gov.

Electronic Supplementary Material: Supplementary material (calculation of average number of encapsulated cytarabine molecules per liposome, FTIR measurements and supplementary discussion) is available in the online version of this article at https://doi.org/10.1007/s12274-018-2202-x (automatically inserted by the publisher).

Keywords

Tapping PTIR; nanoscale chemical imaging; liposomes; cytarabine; drug delivery; nanocarriers

1 Introduction

Efforts to develop novel nanoparticle-based therapeutic paradigms to provide selective drug delivery, disease diagnosis and monitoring of the therapeutic response [1–4] have yielded several clinically approved formulations, particularly for theranostic applications [5]. For example, liposomes [6,7] consist of spherical lipid bilayers that are effective in encapsulating and transporting hydrophilic cargos. The liposomes' lipid composition can be easily customized while their surface can be functionalized with a variety of ligands/ adjuvants like antibodies, polyethylene glycol (PEG), carbohydrates, etc. that enhance bloodstream stability and/or add chemical functions tailored towards clinical targets [8,9]. Liposomes' chemical versatility, biocompatibility and biodegradability, make them ideal carriers for transporting and delivering otherwise difficult to administer therapeutics [10–16], such as short-lived compounds [15], toxic anticancer drugs [14,17,18], vaccines [19], genes [20,21] etc., as highlighted by the growing number of clinically approved formulations [22]. For example, liposomal cytarabine is clinically approved for treating of lymphomatous meningitis [23]. Cytarabine – or cytosine arabinoside (ara- C) - is a chemotherapeutic drug that stops cancer growth by interfering with DNA synthesis by virtue of its close structural/ chemical similarity to the DNA nucleoside cytosine deoxyribose [24]. Because liposomes increase the delivery precision of toxic compounds to cancer sites with respect to disease-free tissues, one of their primary benefits is the reduction of side effects [25]. The synergistic interaction with other nanoparticles in vivo [3,26]. can even further augment liposomal drug delivery precision. Ultimately, delivering anticancer drugs with greater specificity enables reduction of the therapeutic dose significantly, provided that the drug encapsulation efficacy in the carrier is known. Batch to batch reproducibility of nanoparticle properties and composition is critically important for their approval and efficacy in clinical applications, requiring both high throughput and single particle composition-sensitive characterization methods [27–29]. Bulk assays such as high pressure liquid chromatography [30], nuclear magnetic resonance [31] or capillary electrophoresis [32] are commonly employed to assess encapsulation efficiency. However, measurements on single vesicles typically require labelling with fluorescent dyes [28,33]. Consequently, there is an unfulfilled need for label-free methods capable of measuring the composition of small (typically <100 nm) individual liposomes with high spatial resolution. Here, we leverage the photothermal induced resonance (PTIR) technique, a near-field infrared (IR) spectroscopic method, to obtain chemical images and spectra of individual cytarabine-loaded liposomes with nanoscale resolution. PTIR experiments in contact mode, the legacy implementation of this technique, are compared with PTIR experiments leveraging a novel heterodyne detection scheme and AFM tapping-mode operation. Both methods enable discrimination of cytarabine-loaded and empty liposomes as well as the visualization of the cytarabine nanoscale distribution in individual liposomes. However, because liposomes are very soft, they can be easily damaged in contact-mode and expert supervision is necessary to exclude imaging artefacts due to heterogeneities in the local PTIR transduction efficiency. In contrast, we find that the new

tapping-mode PTIR imaging method is better adapted for characterizing mechanically compliant (soft) samples, extending the boundaries of this versatile characterization technique. PTIR's exceptional sensitivity is highlighted by the ability to detect ≈1.7 zmol of cytarabine (≈ 10^3 molecules) label-free and non-destructively.

2. Experimental

2.1. Liposome preparation

All the chemicals were used as received from commercial sources. Liposomes composed of hydrogenated L-α-phosphatidylcholine (HSPC), cholesterol (Chol) and 1,2-dioctadecanoyl-s_n-glycero-3-phosphoethanolamine (PE (18:0 / 18:0), DSPE) with 5.7 : 3.8 : 0.5 (HSPC : Chol : DSPE) molar ratio were prepared according to the thin lipid film hydration technique [34–36]. Sodium phosphate (≥ 99.5 %; 15 mmol L^{-1}, pH 7.4) and NH_4OAc (≥99.99%; 40 mmol L^{-1}, pH 8.4) filtered through a 0.2 μm pore size syringe filter were used for vesicle preparation. Cytarabine (cytosine β-D-arabinofuranoside, ≥ 90 %) from a 40 mmol L^{-1} stock in 40 mmol L^{-1} NH_4OAC (pH 8.4) or 50 mmol L^{-1} stock in 15 mmol L^{-1} sodium phosphate (pH 7.4) was used. Hydration of the lipid film was either performed with (i) 1 mL NH_4OAc, (ii) 1 mL NH_4OAc including cytarabine (40 mmol L^{-1}), (iii) 1 mL sodium phosphate or (iv) 1 mL sodium phosphate including cytarabine (50 mmol L^{-1}). The hydration procedure yielded dispersions of 10 mmol L^{-1} total lipid concentration, which were extruded 21 times through two pre-wetted polycarbonate membranes (100 nm nominal pore size) to obtain small unilamellar liposomes.

Prior to the nES-GEMMA separation and collection on the substrate, all non-encapsulated material was removed from the vesicles via spin filtration [37] employing a polyethersulfone membrane (10 kDa molecular weight cut-off spin filter). Based on the measured weights prior to and post spin filtration, a 1:10 [v:v] dilution of the initial stock was achieved (i.e. the samples had a final lipid concentration of 1 mmol L^{-1}).

2.2. nES GEMMA collection

The nES GEMMA (nano-electrospray gas-phase electrophoretic mobility molecular analysis) set-up [38] consists of a commercially available nES aerosol generator equipped with a ^{210}Po α-particle source, a nano differential mobility analyzer (nDMA) and a n-butanol-based ultrafine condensation particle counter (CPC). A 25 μm inner diameter, fused silica capillary with a homemade tip [39] was used for generation of a stable Taylor cone. A fresh capillary was employed for each day of measurement to preclude cross-contamination of the liposome samples. 0.1 L min^{-1} CO_2 and 1 L min^{-1} compressed, particle-free air at a pressure difference of 28 kPa (4 PSId) were employed for transporting the analytes via the capillary through the neutralization chamber and to the nDMA unit. Particle-free air was additionally dried prior to application. Size-selected liposomes were collected on substrates after particle passage through the nDMA via an electrostatic nanometer aerosol sampler (ENAS) at −3 kV to −3.1 kV voltage on the inner collector rod and 1.5 L min^{-1} sheath air flow rate for 120 min (liposomes with acetate buffer) selecting an EM diameter of 85 nm. Collection of liposomes with phosphate buffer was done similarly but the air flow was held for 180 min (80 nm of EM diameter).

2.3. Liposome preparation

The setup used in this work consists of a commercial PTIR instrument coupled to a commercial external cavity quantum cascade laser array tunable from 1130 cm^{-1} to 1930 cm^{-1}. Contact-mode PTIR experiments were carried out using gold coated cantilevers with 13 kHz ± 4 kHz nominal resonance frequency and with a nominal spring constant between 0.07 N m^{-1} and 0.4 N m^{-1}. Contact-mode spectra were obtained by matching the laser repetition rate to the cantilever second contact resonance frequency by sweeping the laser wavelength at 2 cm^{-1} intervals while maintaining the probe position fixed. Contact-mode maps were obtained by raster scanning the probe while illuminating the sample with a fixed wavelength and using a phase locked loop (PLL) to maintain the resonance excitation condition on the second or third cantilever mode.

For tapping-mode PTIR experiments, a commercial digital lock-in amplifier interfaced with the PTIR instrument was used to demodulate the amplitude at $|f_1 \pm f_{laser}|$ from the cantilever deflection signal. First, using a piezoelectric actuator the cantilever was shaken to identify the first (f_1) and second (f_2) cantilever modes (Fig. 3(a)). The laser frequency was first set tentatively as $f_{laser} = f_2 - f_1$. The laser repetition rate in the tapping-mode PTIR experiments was refined by determining the maximum of the lock-in amplifier demodulated output (at f_2) when sweeping it across a frequency range centered around the f_{laser} first guess value. Tapping-mode PTIR experiments were obtained using gold coated cantilevers with 75 kHz ± 15 kHz nominal resonance frequency and a nominal spring constant between 1 N m^{-1} and 7 N m^{-1}.

2.4. ATR FTIR reference measurements

A commercially available FTIR spectrometer equipped with a DLaTGS (deuterated L-alanine doped triglycerine sulfate) detector and a commercial diamond ATR element (single reflection) was employed for ATR FTIR reference measurements. Spectra were recorded as co-addition of 100 scans with a spectral resolution of 2 cm^{-1}.

2.5. FTIR Transmission measurements

A commercially available spectrometer equipped with a liquid nitrogen cooled MCT (mercury cadmium telluride) detector was employed for transmission measurements in a flow cell (27 μm path length) connected to a commercial syringe pump with a 500 μl glass syringe. For all spectra, 100 scans were co-added with a spectral resolution of 2 cm^{-1}.

3. Results and Discussion

The liposomes investigated here are composed of three different lipids: hydrogenated L-α-phosphatidylcholine (HSPC), cholesterol (Chol) and 1,2-dioctadecanoyl-sn-glycero-3-hosphoethanolamine (DSPE) with 5.7 : 3.8 : 0.5 HSPC : Chol : DSPE molar ratio. Liposomes loaded with cytarabine and buffer solution (either ammonium acetate or phosphate buffer), or liposome filled with buffer solution only (hereafter buffer-loaded liposomes) were prepared according to a thin film hydration method [34,40] followed by an extrusion step (polycarbonate filter, 100 nm nominal pore size) to generate small unilamellar liposomes. Ammonium acetate buffer was used forthe first set of experiments (Fig. 1 and 2)

as part of an established protocol [35,36], but was substituted later with phosphate buffer because of its transparency in the IR range (see Fig. S-1 in the ESM). Size-selected liposomes (85 nm ± 3 nm or 80 nm ± 2 nm particle diameter loaded with ammonium acetate and phosphate buffer respectively) were collected on ZnSe and template stripped gold substrates via nES GEMMA (nano-electrospray gas-phase electrophoretic mobility molecular analysis) [38] for subsequent PTIR measurements. In the collection and size selection process, the particles are injected via electrospray ionization and separated according to their electrophoretic mobility (proportional to the particle size) in a tunable electric field [41]. Throughout the manuscript, the uncertainties in the liposomes' diameters represent a single standard deviation based on the nES GEMMA manufacturer specifications which are in good agreement with previous reports [41]. This liposome production method was chosen to ensure the deposition of intact liposomal nanocarriers, which have otherwise the tendency to burst when deposited on a substrate with other methods [35]. After deposition, the liposome shape typically changes from spherical to ellipsoidal (Fig. 1(c) and 2(a)) with ≈100 nm to ≈ 200 nm widths and ≈ 35 nm to ≈ 50 nm thicknesses, as measured by AFM.

First, FTIR and PTIR reference spectra of buffer-loaded liposomes and pure cytarabine in various forms (see Fig. S-2 in the ESM) were used to identify chemically representative marker bands for cytarabine and liposomes. The C=0 stretch vibration (1734 cm^{-1}) [42] of the liposome constituent lipids was chosen as the liposome marker band because of its strong intensity and because it does not spectrally overlap with the IR bands of cytarabine and buffer. Similarly, the band at 1528 cm^{-1} (C=N and C=C vibration of pyrimidines [24,43]) was selected as the cytarabine marker band.

By combining IR spectroscopy composition sensitivity with atomic force microscopy (AFM) resolution, PTIR, also known as AFM-IR, provides direct and label-free access to molecule-specific information at the nanoscale [44][45]. In PTIR, a portion of the analyte, centered around the AFM tip, is illuminated by a pulsed wavelength-tunable laser (Fig. 1(a)). The absorption of a light pulse in the sample prompts its fast thermal expansion and induces cantilever oscillations with an amplitude (measured by the AFM deflection sensor) proportional to the absorbed energy [46,47]. In PTIR the AFM probe serves as a near-field mechanical detector, enabling nanoscale spectroscopy from the IR to the visible range [48]. Although, the PTIR spatial resolution is typically a weak function of the sample thermomechanical properties, a spatial resolution below 50 nm is routinely obtained [45,48,49]; with resolution down to ≈ 20 nm in contact-mode PTIR [48]. The tapping-mode PTIR experiments reported here indicate a spatial resolution of ≈ 10 nm (see below). In principle, the PTIR technique is of broad applicability because of the demonstrated proportionality between the PTIR signal and the absorption coefficient [46], as in FTIR. PTIR has successfully characterized a wide range of materials e.g. solar cells [50,51], photodetectors [52], pharmaceutics [53], art conservation [54], polymers [55–57], plasmonic structures [58–60], metal-organic frameworks [61] and 2D materials [62,63]. In life sciences applications, PTIR has enabled the investigation of protein secondary structure [64,65], single cells [66], lipids [67,68] and recently, polymeric nanoparticles [69] and hybrid lipid-polymer films [70,71] for drug delivery. Furthermore, PTIR operation in water has been recently demonstrated [72,73], enabling conformational analysis of molecules at the

nanoscale and in their native environment [72]. Recent reviews comparing PTIR with other near-field techniques, such as scattering scanning near field microscopy (s-SNOM) and tip-enhanced Raman spectroscopy (TERS) are available elsewhere [44,74]. Briefly, in contrast with TERS and s-SNOM, which are primarily surface sensitive techniques, PTIR probes samples throughout their thicknesses even in excess of 1 μm [47,75] and it necessitates the probe's plasmonic enhancement only to measure very thin (< 50 nm) samples. This PTIR characteristic, for example, has enabled characterization of live cells [75] and visualizing viral infection at various staged in single bacteria [76].

Dazzi et al. developed a theory for the PTIR signal (S_{PTIR}) generation, that factorizes the PTIR signal transduction into a series of multiplicative contributions [46]; rewritten here, for convenience, using the notation of Ramer et al. [77]:

$$S_{PTIR}(\lambda) \propto H_{AFM} H_m H_{th} H_{opt}(\lambda) I_{inc}(\lambda) \quad (1)$$

Where H_{AFM} is the cantilever contribution (a function of the cantilever modal stiffness, frequency, etc.), $H_m = k_{t-s} \cdot \alpha \cdot z$ is the mechanical contribution (a function of the tip-sample contact stiffness – k_{t-s}, of the sample thermal expansion coefficient – α and thickness – z), H_{th} is the thermal contribution, (a function of the sample thermal properties), H_{opt} is the optical contribution (due to the sample absorptance i.e. a function of the sample complex refractive index) and I_{inc} is the laser incident power, typically measured in a background spectrum. Although the shape of PTIR spectral profiles are determined by the sample optical properties (H_{opt}), the thermomechanical properties of sample and AFM probe ($H_{AFM}H_mH_{th}$) influence the overall PTIR signal intensity [77] making some samples (i.e. with small z or low α or low k_{t-s}) more challenging to measure [78,79]. For example, Barlow et al. observed that for stiffer bacteria on top of softer and more damping polymer layer the PTIR amplitude due to the polymer absorption was stronger when the tip was above the bacteria than when directly over the polymer layer. Since the $H_{AFM}H_mH_{th}$ term in Eq. 1 is wavelength independent (i.e. has the same value in a given location in subsequent PTIR images), ratios of PTIR images can obviate to this PTIR mechanical transduction artefact [79].

The liposomes' very low stiffness hampers the PTIR signal transduction and predisposes them to tip damage in contact-mode. The low stiffness in combination with the liposome small thickness makes these samples challenging to measure with PTIR. Here, we leverage resonance-enhanced PTIR (RE-PTIR) [49] to increase the PTIR sensitivity. Although, RE-PTIR was originally developed for contact-mode AFM, a novel heterodyne detection scheme (explained below) allows resonance enhancement in tapping mode (tapping-mode PTIR).

In contact-mode PTIR experiments [49], the legacy implementation of the technique, the laser repetition rate was tuned to match the frequency of one of the cantilever oscillation modes (≈ 160 kHz, Fig. 1(b)). Because for a given cantilever spring constant (k_C) and free resonance frequency (f_0), the cantilever contact resonance frequencies (f_{res}) depend on the local tip-sample contact stiffness (k_{t-s}) according to the following (simplified) relationship [80]:

$$\frac{f_{res}}{f_0} = \sqrt{\frac{k_C + k_{t-s}}{k_C}} \quad (2)$$

methods, such as a phase locked loop (PLL), are necessary to maintain the resonance enhanced condition throughout the scans [81]. For PTIR tapping-mode experiments, which reduce the likelihood of tip-sample damage, resonant excitation was obtained using a heterodyne detection scheme (see below) which doesn't require resonance tracking because of the weak dependence of the tapping-mode resonance frequencies on the sample's mechanical properties. All the PTIR experiments were obtained by illuminating the sample from the air side (≈ 20° from the sample plane) using p-polarization and gold-coated Si probes.

To illustrate the challenges provided by the liposome samples to PTIR measurements when the tip is in contact, we first measured liposomes containing only the ammonium acetate buffer solution, Fig. 1. Counterintuitively, the PTIR image of the liposome marker band (1734 cm^{-1}, Fig. 1(d)) displays lower signal intensity in the liposome locations than on the substrate. This effect is attributed to the inefficiency of PTIR signal transduction due to the weaker sample-tip force transfer and higher damping on the liposomes (Fig. 1(b)), similarly to what previously observed by Barlow et al. [79]. Since the ZnSe substrate is transparent, to calculate image ratios (Fig. 1(f)) we reference our measurements to the spatially unspecific background absorption at 1260 cm^{-1} attributed to SiO_2 absorption [82] in the AFM cantilever (Fig. 1(e)). Although this operation is relatively straightforward in non-resonantly excited PTIR experiments [79], its implementation with RE-PTIR requires careful supervision, because of the abrupt f_{res} variations observed when the tip is in contact with the liposomes or substrate. While the PLL does not compensate for Q-factor variations, it is effective to maintain the cantilever resonant excitation by adjusting the laser repetition rate, provided that the PTIR signal is well above the noise level - a condition difficult to achieve on these liposome samples. If tracking is lost, the PTIR signal is not properly scaled making the PTIR map not suitable for the image ratio procedure (at least for the pixels where the PLL is ineffective).

Next, we measure liposomes loaded with cytarabine (Fig. 2). On this sample, the low PTIR signal intensity at 1528 cm^{-1} (cytarabine marker), makes resonance tracking particularly hard to maintain throughout an image. However, this problem can be obviated in part by restricting the PLL tracking range to include the liposome contact resonance frequency but exclude the substrate contact resonance frequency. Because the k_{t-s} dependence of the contact resonance is stronger for higher order modes [80], the third cantilever mode was used for these measurements to ensure that the contact resonance frequency of substrate and liposomes were sufficiently separated. This scheme enables reliable frequency tracking on the liposome (the sample of interest) and reaches the upper limit of the PLL range on the ZnSe substrate (see Fig. 2(d), (e)). Subsequently, the ZnSe areas, identified by the frequency map, are carefully excluded from data processing and interpretation.

Using the range-restricted contact resonance tracking the PTIR images at 1528 cm^{-1} (cytarabine marker band; see Fig. 2(b)) and at 1734 cm^{-1} (liposome band; see Fig. 2(c)) highlight cytarabine distribution in the liposome center. This interpretation is confirmed by the PTIR spectra (Fig. 2(g)). Consistently, the spectrum in the liposome periphery displays only the spectral features of the lipids, while the spectrum in the center of the liposome shows additional cytarabine bands. Such heterogeneity is further evidenced by the contact resonance image (see Fig. 2(d)) which shows higher frequencies on the substrate, lower frequencies on the soft liposome periphery and intermediate frequencies in the middle of the liposome (see Fig. 2(e)); indicating that the central region is harder than the liposome shell. Because the soft liposome is deformed by consecutive contact-mode images (see changes of liposome contour in Fig. 2(b), (c) and Fig. S-3) the edges of the liposomes have been excluded from the estimation of the PTIR image ratio (Fig. 2(f)) which, once again, reveals the cytarabine distribution inside a single liposome.

AFM measurements of soft samples are often carried out in tapping mode to avoid sample deformation and/or irreversible sample damage [83]. Therefore, next we leverage the new tapping-mode PTIR method to characterize optimized liposomal nanocarriers (phosphate buffer instead of ammonium acetate buffer, see supporting information) deposited on a gold substrate to augment the PTIR signal intensity [49]. Tapping mode PTIR images were obtained with heterodyne detection (a measurement scheme that enables resonant excitation by non-linear mixing of the cantilever oscillation modes) [84] by setting the laser repetition rate ($f_{laser} \approx 290$ kHz) to match the difference between the second ($f_2 \approx 344$ kHz) and first ($f_1 \approx 54$ kHz) bending modes of the AFM cantilever (Fig. 3(a)). In practice, the cantilever tapping frequency was f_1 and the heterodyne detection was measured at f_2. The tapping-mode PTIR image ratios (Fig. 3(b)) of the chemically specific marker bands (cytarabine: 1528 cm^{-1}; liposome: 1734 cm^{-1}) clearly highlight cytarabine localization at the center of the nanocarrier but not in the controls containing only the buffer (Fig. 3(c)), indicating that tapping-mode PTIR can successfully classify drug-free and drug-loaded liposomes. An additional representative PTIR image of a cytarabine loaded liposome is reported in the supporting information (Fig. S-4). Figure S-5 of the supporting information highlights the good reproducibility of the PTIR images obtained in tapping-mode, even for samples that are easily damaged in contact mode (see Fig. S-3). Furthermore, the tapping-mode PTIR images reveal a spatial resolution of ≈ 10 nm, defined as the distance (Δx) over which the PTIR signal changes from 80% to 20% of the maximum value (Fig 3 f), which is better than the highest spatial resolution reported for contact-mode PTIR (≈ 20 nm) [48]. Based on capillary electrophoresis bulk measurements of the cytarabine concentration inside the liposomes (see supporting information) we estimate an average cytarabine concentration of $\approx 1.7 \times 10^{-21}$ mol or $\approx 10^3$ molecules inside a single nanocarrier. The PTIR measurements presented here are close to the limit of what currently possible; however, the ultimate PTIR limit of detection for cytarabine molecules cannot be obtained with precision because of the uncertainty on the number of cytarabine molecules encapsulated in any given nanocarrier (see table S-1). Nevertheless, these measurements demonstrate an impressive sensitivity, comparable to the lowest PTIR detection limit (≈ 300 molecules), reported for self-assembled monolayers [49], which however, are characterized by a much higher tip-sample contact stiffness (i.e. more amenable to PTIR characterization).

4. Conclusion

In summary, resonance enhanced contact-mode PTIR imaging of soft samples is challenging because of the inefficient PTIR signal transduction, difficulty to maintain resonance excitation and risk for sample damage or deformation. However, careful adaptation of parameter settings and data processing based on detailed understanding of the tip-sample interaction can yield suitable PTIR images that enable the visualization of the cytarabine distribution inside individual liposomes. In contrast, by avoiding sample damage and mechanical artefacts the novel ability to measure PTIR images in tapping-mode can more easily and clearly classify empty and drug loaded liposomes, with the added benefit of increased (≈ 2- to ≈ 5-fold) measurement throughput, based on the scan rate practically achievable. The detection of an estimated ≈ 1.7 zmol of cytarabine inside individual liposomes highlights the impressive PTIR sensitivity and enables, for the first time, measuring the drug distribution inside a single nanocarrier directly (i.e. label free) with a chemically sensitive spectroscopic method, non-destructively and at room temperature. Beyond the proof of concept presented here, extensive studies to determine the distribution and quantification of chemotherapeutic drug-loading in liposomal nanocarriers will benefit from improvements in the PTIR signal-to-noise ratio and throughput. Incremental advances could be obtained by leveraging different combinations of cantilever modes for PTIR heterodyne detection. Alternatively, a more disruptive approach involves the use of novel nanoscale optomechanical AFM transducers [85] that have been shown to increase the PTIR sensitivity (50-fold) and throughput (> 2500-fold) compared to conventional AFM cantilevers without the need for resonant excitation [85]. We believe that such transducers hold great promise to further aid the development of liposome formulations towards clinical applications. This study lays the foundation for the quantification of drug-loading in single liposomes; a longstanding goal that could potentially improve the quality control for drug delivery systems and ultimately contribute to minimize side effects of highly toxic drugs.

Supplementary Material

Refer to Web version on PubMed Central for supplementary material.

Acknowledgements

K.W., G.R. and A.C. wrote the manuscript with inputs from V.U.W., G.A. and B.L. G.A., B.L. and A.C. supervised the project. K.W. performed and evaluated contact- and tapping-mode PTIR measurements with support from G.R. and A.C. V.U.W. prepared liposomes and performed nES-GEMMA collection. All authors discussed the results and commented on the manuscript. K.W. acknowledges financial support by the Austrian research funding association (FFG) within the research project “NanoSpec – High-resolution near-field infrared microscopy for the process control of nanotechnological components” (contract#843594). G.R. acknowledges support from the University of Maryland through the Cooperative Research Agreement between the University of Maryland and the National Institute of Standards and Technology Center for Nanoscale Science and Technology, Award 70NANB14H209. The authors thank Mohit Tuteja and Brian Hoskins for fruitful discussions.

References

[1]. Boisselier E; Astruc D Gold nanoparticles in nanomedicine: preparations, imaging, diagnostics, therapies and toxicity. Chem. Soc. Rev, 2009, 38, 1759–1782. [PubMed: 19587967]

[2]. Allen TM; Cullis PR, Liposomal drug delivery systems: From concept to clinical applications. Adv. Drug Deliv. Rev, 2013, 65, 36–48. [PubMed: 23036225]

[3]. Von Maltzahn G; Park J; Lin KY; Singh N; Schwöppe C; Mesters R; Berdel WE; Ruoslahti E; Sailor MJ; Bhatia SN Nanoparticles that communicate in vivo to amplify tumour targeting. Nat. Mater, 2011, 10, 545–552. [PubMed: 21685903]

[4]. Lee D-E; Koo H; Sun I-C; Ryu JH; Kim K; Kwon IC Multifunctional nanoparticles for multimodal imaging and theragnosis. Chem. Soc. Rev, 2012, 41, 2656–2672. [PubMed: 22189429]

[5]. Thakor AS; Gambhir SS Nanooncology: The Future of Cancer Diagnosis and Therapy. CA - A Cancer J. Clin, 2013, 63, 395–418.

[6]. Senapati S; Kumar Mahanta A; Kumar S; Maiti P Controlled drug delivery vehicles for cancer treatment and their performance. Nat. Signal Transduct. Target. Ther, 2018, 3, 7.

[7]. Lammers T; Hennink WE; Storm G Tumour-targeted nanomedicines : principles and practice. Br. J. Cancer, 2008, 99, 392–397. [PubMed: 18648371]

[8]. Peer D; Karp JM; Hong S; Farokhzad OC; Margalit R; Langer R Nanocarriers as an emerging platform for cancer therapy. Nat. Nanotechnol, 2007, 2, 751–760. [PubMed: 18654426]

[9]. Torchilin VP Recent advances with liposomes as pharmaceutical carriers. Nat. Rev. Drug Discov, 2005, 4, 145–160. [PubMed: 15688077]

[10]. Morton SW; Lee MJ; Deng ZJ; Dreaden EC; Siouve E; Shopsowitz KE; Shah NJ.; Yaffe MB; Hammond PT A Nanoparticle-Based Combination Chemotherapy Delivery System for Enhanced Tumor Killing by Dynamic Rewiring of Signaling Pathways. Sci. Signal, 2014, 7, ra44. [PubMed: 24825919]

[11]. Zhang Y; Chan HF; Leong KW Advanced materials and processing for drug delivery : The past and the future. Adv. Drug Deliv. Rev, 2013, 65, 104–120. [PubMed: 23088863]

[12]. Venditto VJ; Szoka FC Jr Cancer nanomedicines : So many papers and so few drugs ! Adv. Drug Deliv. Rev, 2013, 65, 80–88. [PubMed: 23036224]

[13]. Allen TM; Cullis PR. Liposomal drug delivery systems : From concept to clinical applications. Adv. Drug Deliv. Rev, 2013, 65, 36–48. [PubMed: 23036225]

[14]. Sercombe L; Veerati T; Moheimani F; Wu SY; Hua S Advances and Challenges of Liposome Assisted Drug Delivery. Front. Pharmacol, 2015, 6, 286. [PubMed: 26648870]

[15]. Young SA; Smith TK Lipids and Liposomes in the Enhancement of Health and Treatment of Disease In Drug Discovery and Development - From Molecules to Medicine, InTech, 2015; pp 133–162.

[16]. Bozzuto G; Molinari A Liposomes as nanomedical devices. Int. J. Nanomedicine, 2015, 10, 975–999. [PubMed: 25678787]

[17]. Caldeira S; Lopes DA; Ferreira S; Leite EA; Oliveira MC Liposomes as Carriers of Anticancer Drugs In Cancer Treatment - Conventional and Innovative Approaches, InTech, 2013; pp 85–124.

[18]. Cagdas M; Sezer AD; Bucak S Liposomes as Potential Drug Carrier Systems for Drug Delivery In Application of Nanotechnology in Drug Delivery; InTech, 2014; pp 1–50.

[19]. Schwendener RA Liposomes as vaccine delivery systems : a review of the recent advances. Ther. Adv. Vaccines, 2014, 2, 159–182. [PubMed: 25364509]

[20]. Rasoulianboroujeni M; Kupgan G; Moghadam F; Tahriri M; Boughdachi A; Khoshkenar P Development of a DNA-liposome complex for gene delivery applications. Mater. Sci. Eng. C, 2017, 75, 191–197.

[21]. Saffari M; Reza H; Dass CR Barriers to Liposomal Gene Delivery: from Application Site to the Target. Iran. J. Pharm. Res, 2016, 15, 3–17.

[22]. Bulbake U; Doppalapudi S; Kommineni N; Khan W Liposomal Formulations in Clinical Use: An Updated Review. Pharmaceutics, 2017, 9, 1–33.

[23]. Pillai G Nanomedicines for Cancer Therapy : An Update of FDA Approved and Those under Various Stages of Development. Pharm. Pharm. Sci, 2014, 1, 1–13.

[24]. El-Subbagh HI; Al-Badr AA Profiles of Drug Substances, Excipients, and Related Methodology In Cytarabine; Elsevier Inc: Burlington, 2009; Vol 34, pp 37–113.

[25]. Germain M; Meyre M; Pou L; Paolini M; Berjaud C; Bergere M; Levy L; Pottier A Priming the body to receive the therapeutic agent to redefine treatment benefit/risk profile. Sci. Rep, 2018, 8, 4797. [PubMed: 29556068]

[26]. Park BJ; Von Maltzahn G; Ong LL; Centrone A; Hatton TA; Ruoslahti E; Bhatia SN; Sailor MJ Cooperative Nanoparticles for Tumor Detection and Photothermally Triggered Drug Delivery. Adv. Mater, 2010, 22, 880–885. [PubMed: 20217810]

[27]. Mullen DG; Holl MMB Heterogeneous Ligand-Nanoparticle Distributions: A Major Obstacle to Scientific Understanding and Commercial Translation. Acc. Chem. Res, 2011, 44, 1135–1145. [PubMed: 21812474]

[28]. Lohse B; Bolinger P; Stamou D Encapsulation Efficiency Measured on Single Small Unilamellar Vesicles. JACS Commun., 2008, 130, 14372–14373.

[29]. Ernsting MJ; Murakami M; Roy A; Li S-D Factors Controlling the Pharmacokinetics, Biodistribution and Intratumoral Penetration of Nanoparticles. J. Control. Release, 2013, 172, 782–794. [PubMed: 24075927]

[30]. Ohnishi N; Yamamoto E; Tomida H; Hyodo K; Ishihara H; Kikuchi H; Tahara K; Takeuchi H Rapid determination of the encapsulation efficiency of a liposome formulation using column-switching HPLC. Int. J. Pharm, 2013, 441, 67–74. [PubMed: 23262429]

[31]. Zhang X; Patel AB; De Graaf RA; Behar KL Determination of liposomal encapsulation efficiency using proton NMR spectroscopy. Chem. Phys. Lipids, 2004, 127, 113–120. [PubMed: 14706745]

[32]. Franzen U; Nguyen TTTN; Vermehren C; Gammelgaard B; Østergaard J Characterization of a liposome-based formulation of oxaliplatin using capillary electrophoresis : Encapsulation and leakage. J. Pharm. Biomed. Anal, 2011, 55, 16–22. [PubMed: 21282028]

[33]. Chen C; Zhu S; Wang S; Zhang W; Cheng Y; Yan X Multiparameter Quantification of Liposomal Nanomedicines at the Single-Particle Level by High-Sensitivity Flow Cytometry. ACS Appl. Mater. Interfaces, 2017, 9, 13913–13919. [PubMed: 28374584]

[34]. Jesorka A; Orwar O Liposomes: technologies and analytical applications. Annu. Rev. Anal. Chem, 2008, 1, 801–832.

[35]. Weiss VU; Urey C; Gondikas A; Golesne M; Friedbacher G; Von der Kammer F; Hofmann T; Andersson R; Marko-Varga G; Marchetti-Deschmann M; Allmaier G Nano electrospray gas-phase electrophoretic mobility molecular analysis (nES GEMMA) of liposomes: applicability of the technique for nano vesicle batch control. Analyst, 2016, 141, 6042–6050. [PubMed: 27549027]

[36]. Urey C; Weiss VU; Gondikas A; Von Der Kammer F; Hofmann T; Marchetti-Deschmann M; Allmaier G; Marko-Varga G; Andersson R Combining gas-phase electrophoretic mobility molecular analysis (GEMMA), light scattering , field flow fractionation and cryo electron microscopy in a multidimensional approach to characterize liposomal carrier vesicles. Int. J. Pharm, 2016, 513, 309–318. [PubMed: 27639623]

[37]. Weiss VU; Lehner A; Rerul L; Grombe R; Rratzmeier M; Marchetti-Deschmann M; Allmaier G Characterization of cross-linked gelatin nanoparticles by electrophoretic techniques in the liquid and the gas phase. Electrophoresis, 2013, 34, 3267–3276. [PubMed: 24114950]

[38]. Kaufman SL; Skogen JW; Dorman FD; Zarrin F Macromolecule Analysis Based on Electrophoretic Mobility in Air: Globular Proteins. Anal. Chem, 1996, 68, 1895–1904. [PubMed: 21619100]

[39]. Tycova A; Prikryl J; Foret F Reproducible preparation of nanospray tips for capillary electrophoresis coupled to mass spectrometry using 3D printed grinding device. Electrophoresis, 2016, 37, 924–930. [PubMed: 26626777]

[40]. Bangham AD; Standish MM; Watkins JC Diffusion of Univalent Ions across the Lamellae of Swollen Phospholipids. J. Mol. Biol, 1965, 13, 238–252. [PubMed: 5859039]

[41]. Kinney PD; Pui DYH; Mulholland GW; Bryner NP Use of the Electrostatic Classification Method to Size 0.1 μm SRM Particles - A Feasibiiiy Study. J. Res. Natl. Inst. Stand. Technol, 1991, 96, 147–176. [PubMed: 28184107]

[42]. Lewis RNAH; Mcelhaney RN; Pohle W; Mantsch HH Components of the Carbonyl Stretching Band in the Infrared Spectra of Hydrated 1, 2-Diacylglycerolipid Bilayers : A Reevaluation. Biophys. J, 1994, 67, 2367–2375. [PubMed: 7696476]

[43]. Socrates G Infrared and Raman Characteristic Group Frequencies; John Wiley & Sons, LTD, 2001.

[44]. Centrone A Infrared Imaging and Spectroscopy Beyond the Diffraction Limit. Annu. Rev. Anal. Chem, 2015, 8, 101–126.

[45]. Dazzi A; Prater CB AFM-IR: Technology and Applications in Nanoscale Infrared Spectroscopy and Chemical Imaging. Chem. Rev, 2017, 117, 5146–5173. [PubMed: 27958707]

[46]. Dazzi A; Glotin F; Carminati R Theory of infrared nanospectroscopy by photothermal induced resonance. J. Appl. Phys, 2010, 107, 124519.

[47]. Lahiri B; Holland G; Centrone A Chemical Imaging Beyond the Diffraction Limit: Experimental Validation of the PTIR Technique. Small, 2013, 9, 439–445. [PubMed: 23034929]

[48]. Katzenmeyer AM; Holland G; Kjoller K; Centrone A Absorption Spectroscopy and Imaging from the Visible through Mid- Infrared with 20 nm Resolution. Anal. Chem, 2015, 87, 3154–3159. [PubMed: 25707296]

[49]. Lu F; Jin M; Belkin MA Tip-enhanced infrared nanospectroscopy via molecular expansion force detection. Nat. Photonics, 2014, 8, 307–312.

[50]. Strelcov E; Dong Q; Li T; Chae J; Shao Y; Deng Y; Gruverman A; Huang J; Centrone A CH3NH3PbI3 perovskites : Ferroelasticity revealed. Sci. Adv, 2017, 3, e1602165. [PubMed: 28439542]

[51]. Chae J; Dong Q; Huang J; Centrone A Chloride Incorporation Process in CH3NH3PbI3-xClx Pervoskites via Nanoscale Bandgap Maps. Nano Lett, 2015, 15, 8114–8121. [PubMed: 26528710]

[52]. Dong R; Fang Y; Chae J; Dai J; Xiao Z; Dong Q; Yuan Y; Centrone A; Zeng XC; Huang J High-Gain and Low-Driving-Voltage Photodetectors Based on Organolead Triiodide Perovskites. Adv. Mater, 2015, 27, 1912–1918. [PubMed: 25605226]

[53]. Eerdenbrugh BVAN; Lo M; Kjoller K; Marcott C; Taylor LS Nanoscale Mid-Infrared Imaging of Phase Separation in a Drug – Polymer Blend. J. Pharm. Sci, 2012, 101, 2066–2073. [PubMed: 22388948]

[54]. Morsch S; van Driel BA; van den Berg KJ; Dik J Investigating the Photocatalytic Degradation of Oil Paint using ATR-IR and AFM-IR. Appl. Mater. Interfaces, 2017, 9, 10169–10179.

[55]. Ghosh S; Kouamé NA; Ramos L; Remita S; Dazzi A; Deniset-besseau A; Beaunier P; Goubard F; Aubert P; Remita H Conducting polymer nanostructures for photocatalysis under visible light. Nat. Mater, 2015, 14, 505–511. [PubMed: 25774954]

[56]. Tri PN; Prud'homme RE Nanoscale Lamellar Assembly and Segregation Mechanism of Poly (3-hydroxybutyrate)/ Poly (ethylene glycol) Blends. Macromolecules, 2018, 51, 181–188.

[57]. Morsch S; Liu Y; Lyon SB; Gibbon SR Insights into Epoxy Network Nanostructural Heterogeneity Using AFM-IR. Appl. Mater. Interfaces, 2016, 8, 959–966.

[58]. Chae J; Lahiri B; Centrone A Engineering Near-Field SEIRA Enhancements in Plasmonic Resonators. ACS Photonics, 2016, 3, 87–95. [PubMed: 27182532]

[59]. Lahiri B; Holland G; Aksyuk V; Centrone A Nanoscale Imaging of Plasmonic Hot Spots and Dark Modes with the Photothermal-Induced Resonance Technique. Nano Lett, 2013, 13, 3218–3224. [PubMed: 23777547]

[60]. Katzenmeyer AM; Chae J; Kasica R; Holland G; Lahiri B; Centrone A Nanoscale Imaging and Spectroscopy of Plasmonic Modes with the PTIR Technique. Adv. Opt. Mater, 2014, 2, 718–722.

[61]. Katzenmeyer AM; Canivet J; Holland G; Farrusseng D; Centrone A Assessing Chemical Heterogeneity at the Nanoscale in Mixed-Ligand Metal-Organic Frameworks with the PTIR Technique. Angew. Chemie (International ed.), 2014, 53, 2852–2856.

[62]. Brown LV; Davanco M; Sun Z; Kretinin A; Chen Y; Matson JR; Vurgaftman I; Sharac N; Giles AJ; Fogler MM; Taniguchi T; Watanabe K; Novoselov KS; Maier SA; Centrone A; Caldwell JD Nanoscale Mapping and Spectroscopy of Nonradiative Hyperbolic Modes in Hexagonal Boron Nitride Nanostructures. Nano Lett, 2018, 18, 1628–1636. [PubMed: 29451802]

[63]. Rosenberger MR; Wang MC; Xie X; Rogers JA; Nam S; King WP Measuring individual carbon nanotubes and single graphene sheets using atomic force microscope infrared spectroscopy. Nanotechnology, 2017, 28, 355707. [PubMed: 28656907]

[64]. Ramer G; Balbekova A; Schwaighofer A; Lendl B Method for Time-Resolved Monitoring of a Solid State Biological Film Using Photothermal Infrared Nanoscopy on the Example of Poly-L-Lysine. Anal. Chem, 2015, 87, 4415–4420. [PubMed: 25809862]

[65]. Ruggeri FS; Habchi J; Cerreta A; Dietler G AFM-Based Single Molecule Techniques: Unraveling the Amyloid Pathogenic Species. Curr. Pharm. Des, 2016, 22, 3950–3970. [PubMed: 27189600]

[66]. Dazzi A; Prater CB; Hu Q; Chase BD; Rabolt JF; Marcott C AFM – IR: Combining Atomic Force Microscopy and Infrared Spectroscopy for Nanoscale Chemical Characterization. Appl. Spectrosc. OA, 2012, 66, 1365–1384.

[67]. Marcott C; Lo M; Kjoller K; Balooch G; Luengo GS Localization of Human Hair Structural Lipids Using Nanoscale Infrared Spectroscopy and Imaging. Appl. Spectrosc, 2014, 68, 564–569. [PubMed: 25014600]

[68]. Yarrow F; Kennedy E; Salaun F; Rice JH Sub-wavelength infrared imaging of lipids. Biomed. Opt. Express, 2011, 2, 37–43.

[69]. Pancani E; Mathurin J; Bilent S; Dazzi A; Deniset-besseau A; Gref R High-Resolution Label-Free Detection of Biocompatible Polymeric Nanoparticles in Cells. Part. Part. Syst. Charact, 2018, 1700457.

[70]. Kang M; Tuteja M; Centrone A; Topgaard D; Leal C Nanostructured Lipid-Based Films for Substrate-Mediated Applications in Biotechnology. Adv. Fund. Mater, 2018, 28, 1704356.

[71]. Tuteja M; Kang M; Leal C; Centrone A Nanoscale partitioning of paclitaxel in hybrid lipid–polymer membranes. Analyst, 2018, 143, 3808–3813. [PubMed: 29878001]

[72]. Ramer G; Ruggeri FS; Levin A; Knowles TPJ; Centrone A Determination of Polypeptide Conformation with Nanoscale Resolution in Water. ACS Nano, 2018, 12, 6612–6619. [PubMed: 29932670]

[73]. Jin M; Lu F; Belkin MA High-sensitivity infrared vibrational nanospectroscopy in water. Light Sci. Appl, 2017, 6, e17096. [PubMed: 30167276]

[74]. Xiao L; Schultz ZD Spectroscopic Imaging at the Nanoscale: Technologies and Recent Applications. Anal. Chem, 2018, 90, 440–458. [PubMed: 29028297]

[75]. Mayet C; Dazzi A; Prazeres R; Allot F; Glotin F; Ortega JM Sub-100 nm IR spectromicroscopy of living cells. Opt. Lett, 2008, 33, 1611–1613. [PubMed: 18628814]

[76]. Dazzi A; Prazeres R; Glotin F; Ortega JM; Al-Sawaftah M; de Frutos M Chemical mapping of the distribution of viruses into infected bacteria with a photothermal method. Ultramicroscopy, 2008, 108, 635–641. [PubMed: 18037564]

[77]. Ramer G; Aksyuk VA; Centrone A Quantitative Chemical Analysis at the Nanoscale Using the Photothermal Induced Resonance Technique. Anal. Chem, 2017, 89, 13524–13531. [PubMed: 29165992]

[78]. Katzenmeyer AM; Holland G; Chae J; Band A; Kjoller K; Centrone A Mid-infrared spectroscopy beyond the diffraction limit via direct measurement of the photothermal effect. Nanoscale, 2015, 7, 17637–17641. [PubMed: 26458223]

[79]. Barlow DE; Biffinger JC; Cockrell-Zugell AL; Lo M; Kjoller K; Cook D; Lee KW; Pehrsson PE; Crookes-Goodson WJ; Hung C; Nadeau LJ; Russell JN The importance of correcting for variable probe – sample interactions in AFM-IR spectroscopy: AFM-IR of dried bacteria on a polyurethane film. Analyst, 2016, 141, 4848–4854. [PubMed: 27403761]

[80]. Rabe U; Janser K; Arnold W Vibrations of free and surface-coupled atomic force microscope cantilevers : Theory and experiment. Rev. Sci. Instrum, 1996, 67, 3281–3293.

[81]. Ramer G; Reisenbauer F; Steindl B; Tomischko W; Lendl B Implementation of Resonance Tracking for Assuring Reliability in Resonance Enhanced Photothermal Infrared Spectroscopy and Imaging. Appl. Spectrosc, 2017, 71, 2013–2020. [PubMed: 28756704]

[82]. Hu SM Infrared absorption spectra of SiO2 precipitates of various shapes in silicon: calculated and experimental. J. Appl. Phys, 1980, 51, 5945–5948.

[83]. Last JA; Russell P; Nealey PF; Murphy CJ The Applications of Atomic Force Microscopy to Vision Science. Investig. Ophthalmol. Vis. Sci, 2010, 51, 6083–6094. [PubMed: 21123767]

[84]. Tetard L; Passian A; Farahi RH; Thundat T; Davison BH Opto-nanomechanical spectroscopic material characterization. Nat. Nanotechnol, 2015, 10, 870–877. [PubMed: 26258550]

[85]. Chae J; An S; Ramer G; Stavila V; Holland G; Yoon Y; Talin AA; Allendorf M; Aksyuk VA; Centrone A Nanophotonic Atomic Force Microscope Transducers Enable Chemical Composition

and Thermal Conductivity Measurements at the Nanoscale. Nano Lett, 2017, 17, 5587–5594. [PubMed: 28770607]

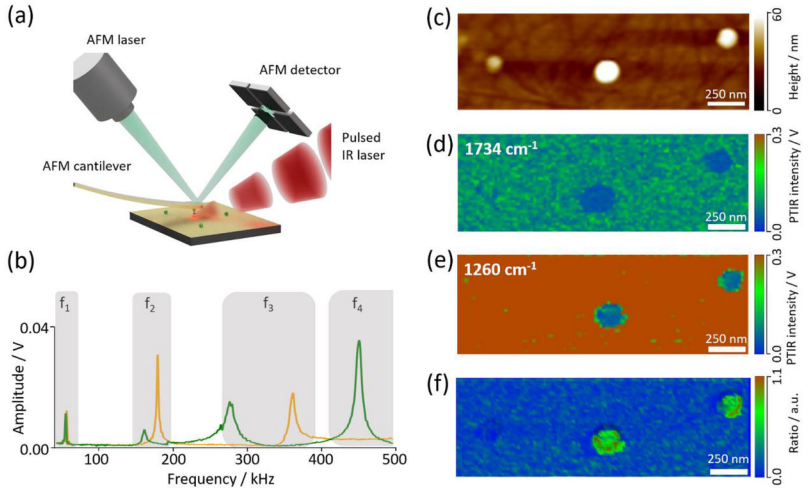

Figure 1.

Contact-mode RE-PTIR measurement schematic and characterization of buffer-loaded liposomes. (a) PTIR measurement schematic: the sample is illuminated from the air side by a pulsed, wavelength-tunable mid-IR laser with tunable repetition rate (red). The IR absorption is detected locally via the cantilever deflection signal. (b) Contact-mode PTIR signal (frequency domain) displaying the intensity of the cantilever resonances excited by the absorption of light pulses when the cantilever is in contact with the sample (green) or the substrate (yellow). In contact-mode RE-PTIR experiments, the laser frequency was set to match either the second (≈ 160 kHz) or third (≈ 270 kHz) cantilever resonance. (c) AFM topography map, (d) PTIR map at 1734 cm^{-1} (liposome marker band), (e) PTIR map at 1260 cm^{-1} (non-specific background) of liposomes loaded with ammonium acetate buffer solution. (f) Because the soft liposomes hamper PTIR signal transduction, the correct distribution of analytes (lipids) is obtained by calculating PTIR ratio maps (1734 cm^{-1} vs 1260 cm^{-1}). The images (0.2 Hz scan rate) were acquired with a PLL bandwidth of ± 8 kHz centered around the cantilever second resonance mode. The pixel size was 17.5 nm in x- and y- directions.

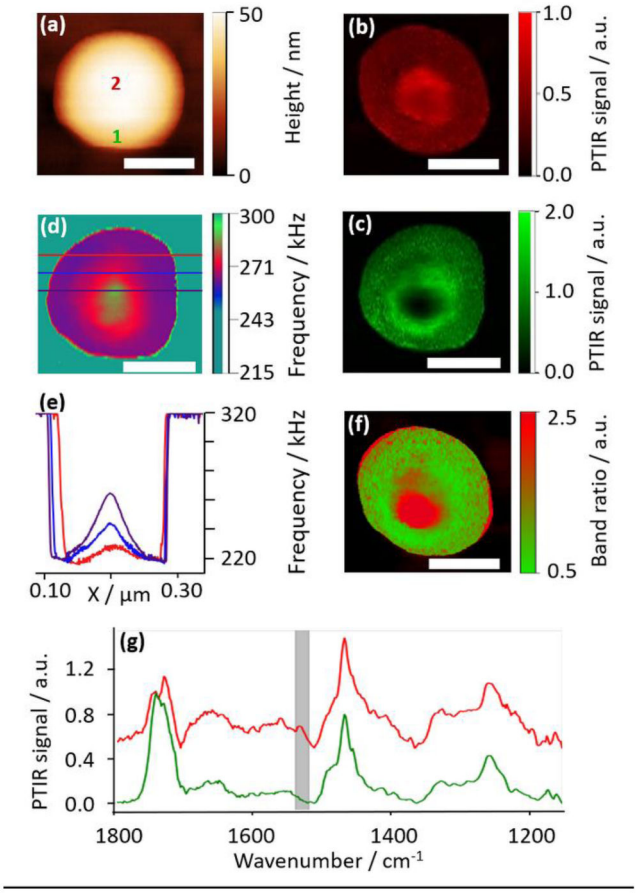

Figure 2.

Contact-mode RE-PTIR characterization of cytarabine-loaded liposomes. (a) AFM topography map, (b) PTIR map at 1528 cm^{-1} (cytarabine), (c) PTIR map at 1734 cm^{-1} (liposome) and (d) contact frequency map (5 parallel lines average) of cytarabine-loaded liposomes. (e) Color-coded line profiles extracted in the marked locations in panel (d) showing higher contact resonance frequencies in the center of the liposome. (f) 1528 cm^{-1} vs. 1734 cm^{-1} PTIR image ratio (i.e. cytarabine vs lipid). Red and green highlight cytarabine rich and lipid rich regions respectively. The images (0.1 Hz scan rate) were acquired using a PLL to track the position of the cantilever third resonance mode (≈ 270 kHz) in the range between 210 kHz and 320 kHz. The pixel size was 0.75 nm and 3 nm in x- and y- directions respectively. (g) PTIR spectra obtained from the color-coded locations in panel (a). The spectrum closer to the liposome center (red) shows the cytarabine characteristic peak (1528 cm^{1}, highlighted in gray) which is absent in the spectrum closer to the liposome edge (green). The spectra are displayed with an offset for clarity. The scale bars are 100 nm.

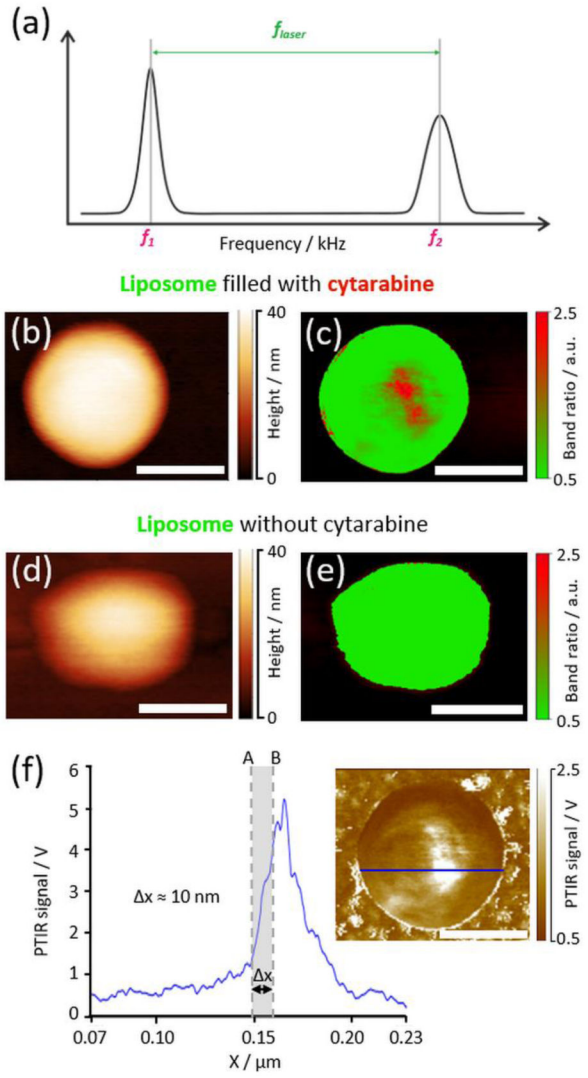

Figure 3.

Tapping-mode PTIR measurements of cytarabine-loaded liposomes and buffer-loaded liposomes. (a) In tapping-mode PTIR experiments, the laser frequency ($f_{laser} \approx 290$ kHz) was set to match the difference between the second ($f_2 \approx 344$ kHz) and first ($f_1 \approx 54$ kHz) bending modes of the AFM cantilever. (b) AFM topography map and (c) 1528 cm^{-1} vs. 1734 cm^{-1} PTIR image ratio (i.e. cytarabine vs lipid) of a cytarabine-loaded liposome. (d) AFM topography map and (e) 1528 cm^{-1} vs. 1734 cm^{-1} PTIR image ratio of a liposome loaded with phosphate buffer only. Red and green colors in the PTIR ratio maps highlight cytarabine rich and lipid rich regions, respectively. (f) Line profile from the 1528 cm^{-1} tapping-mode PTIR map (blue line in the inset) highlighting the high spatial resolution (≈ 10 nm) of this method. The images (0.5 Hz scan rate) have a pixel size of 0.6 nm in the × direction and 2 nm (c) or 3 nm (e) in the y-direction respectively. The scale bars are 100 nm.